Analyst

PAPER

View Article Online
View Journal

Cite this: DOI: 10.1039/d5an00347d

Hydropyrolysis: towards fluorescence-free Raman spectroscopy analysis of internal diesel injector deposits

Joel Viggars,[a] Sarah Angel-Smith,[a] Graham A. Rance,[b,c] Ahmed Khairy,[a,d] Will Meredith,[a] Adrienne Davis,[b] Jim Barker,*[e] Jacqueline Reid,[e] David J. Scurr[f] and Colin E. Snape[a]

Micro-Raman spectroscopy (μRS) is an established analytical tool enabling facile determination of the structural ordering within carbonaceous materials, including the particulate-matter found in vehicle deposits and environmental matrices. However, if fluorescent species are present within the material under examination, μRS analysis can be at best complicated and at worst impossible. Common methods to circumvent this issue, such as changing the excitation laser wavelength and/or photobleaching, are not always possible. In this study, we demonstrate pyrolysis under high hydrogen pressures (hydropyrolysis, HyPy) as an effective thermal treatment for the removal of fluorescent species at relatively low temperatures (350 °C), without significantly altering the structure of the parent carbonaceous material. This was illustrated through μRS investigation of a series of six carbon reference samples, whereby, after HyPy, the interference from fluorescence was significantly reduced, whilst the positions, widths and intensity ratios of the diagnostic D and G bands remained largely unchanged. Application of hydropyrolysis to a series of five internal diesel injector deposits (IDIDs) enabled a μRS investigation of the physicochemical structure of the deposited carbons for the first time. Moreover, mass spectrometry analysis of the volatile species removed during HyPy of IDIDs where engine failures had occurred suggested that linear polyunsaturated *n*-C_{16} and *n*-C_{18} alkenes were likely responsible for the fluorescence. As HyPy can be readily applied to a variety of carbonaceous materials, for example, petroleum source rocks contaminated with drilling muds, the approach we describe here represents a general strategy for fluorescence suppression enabling structural investigation of carbons by μRS.

Received 28th March 2025,
Accepted 21st March 2026

DOI: 10.1039/d5an00347d

rsc.li/analyst

Introduction

Micro-Raman spectroscopy (μRS) is an invaluable tool for materials characterisation providing key information on the structure, chemical composition and local environment of molecules and molecular materials using the diagnostic fingerprint that the vibrational spectrum uniquely delivers. Over the last 50 years, and driven principally by the increasing commercial availability of the laser as an excitation source, μRS has been applied widely across a range of sectors, including life sciences, pharmaceuticals, geology, cosmetics, semiconductors and carbonaceous materials,[1–6] enabling native-state analysis, in the absence of labels or exhaustive preparation procedures, in a non-invasive and non-destructive fashion. Of particular note, the application of μRS for the characterisation of carbonaceous materials has been extensively explored. Enabling facile discrimination of the carbon allotropes, including fullerenes (0D), carbon nanotubes (1D), graphene (2D) and diamond (3D), μRS is now commonly used as a means of quantifying the degree of structural ordering of carbonaceous materials containing graphitic domains. This involves careful analysis of the two most prominent peaks in the first-order Raman spectrum, namely the D and G bands, observed at ~1350 and 1580 cm^{-1} in graphite, respectively,[6–15] providing information complementary to that obtained from ^{13}C nuclear magnetic resonance (NMR) spectroscopy and X-ray diffraction (XRD) analysis,[16–18] but offering the advantages of lower sample requirements and, when inte-

[a]Faculty of Engineering, University of Nottingham, Energy Technologies Building, Innovation Park, Jubilee Campus, Triumph Road, Nottingham NG7 2TU, UK
[b]School of Chemistry, University of Nottingham, University Park, Nottingham, NG7 2RD, UK
[c]Nanoscale and Microscale Research Centre (nmRC), University of Nottingham, University Park, Nottingham, NG7 2RD, UK
[d]Geology Department, Faculty of Science, South Valley University, Qena, 83523, Egypt
[e]Innospec Ltd, Manufacturing Park/Oil Sites Rd, Ellesmere Port, CH65 4EY, UK. E-mail: jim.barker@innospecinc.com
[f]Laboratory of Pharmacy, University of Nottingham, Nottingham NG7 2RD, UK

grated with confocal optics, permitting analysis from volumes approaching the optical diffraction limit.

However, as every analyst who has attempted to record a Raman spectrum will attest, interference from fluorescence can represent a significant problem. Given the sizeable differences in cross-section ($d\sigma_{fluo}/d\Omega \sim 10^{-16}$ cm^2 sr^{-1} for fluorescence emission, $d\sigma_{Raman}/d\Omega \sim 10^{-24}$ cm^2 sr^{-1} for Raman scattering),[19] if a fluorophore is present, either inherent to the molecular species under examination or as an impurity, and closely matches the wavelength of the Raman excitation laser, fluorescence poses a big problem. The contribution of fluorescence to the observed baseline intensity and associated reduction in Stokes Raman signal-to-noise ratio can mask and/or distort the detailed structural information held within the Raman spectrum and may lead to inaccurate conclusions being drawn. Consequently, a number of routes have been explored to solve the fluorescence issue. The most common approach is to change the wavelength of the excitation laser, with longer wavelength (*e.g.*, NIR) lasers – where the photon has insufficient energy to excite strong fluorescence – and shorter wavelength (*e.g.*, UV) lasers – where fluorescence may be excited but the emission is sufficiently separated in energy from Raman scattering that spectral overlap is avoided – both reported as solutions to the fluorescence problem.[20–27] However, this necessitates access to Raman instrumentation with multiple excitation sources, with many instruments typically equipped with only 532 or 785 nm lasers. Photobleaching, a process involving pre-exposure of the sample to the excitation laser prior to spectrum acquisition and resulting in photochemical degradation of the fluorophore, is similarly popular, but must be used with caution, particularly for laser-sensitive materials like carbons. More advanced approaches for fluorescence suppression include time-, frequency- and wavelength-domain and computational methods, the relative merits and limitations of which have been extensively reviewed.[28] However, in general, these approaches are considered expensive in terms of time and cost, involving hardware and/or software not typically found on current commercial μRS systems, and therefore alternative approaches should be considered.

In this study, we explore the application of hydropyrolysis (HyPy) and nitrogen pyrolysis (NPy) for the thermal pre-treatment of carbonaceous samples enabling removal of the species responsible for fluorescence. HyPy involves heating a sample under a stream of high-pressure hydrogen (150 bar)[29–31] achieving a much higher conversion of labile organic matter to volatiles than conventional pyrolysis, as shown across a range of carbonaceous materials, including biomass, petroleum source rocks and coals, whilst preserving the structure of the volatiles due to the use of lower temperature. This has led to a number to applications in petroleum exploration using bound biomarkers released with minimal conformational change. Furthermore, less growth of polyaromatic clusters, leading to char formation in HyPy, compared to NPy, has been reported, enabling the fraction of pyrolytic or black carbon in environmental carbonaceous materials to be determined.[30]

To demonstrate the ability of HyPy and/or NPy to remove fluorescing species and thereby facilitate meaningful μRS analysis of the aromatic structures, we have explored their application across a range of six carbon reference samples, namely graphite, multi-walled carbon nanotubes (MWCNT), graphene oxide (GO), charcoal and two Biochars. Our analysis of these reference samples indicates that in general HyPy treatment has little to no impact on the structure of the carbon but elicits effective fluorescence suppression in cases where this was observed before treatment. Moreover, the application of HyPy for removal of fluorescing species has enabled μRS analysis of Internal Diesel Injector Deposits (IDIDs) for the first time. The worldwide quest to reduce emissions from diesel engines has seen significant demands for increased efficiency and performance from diesel engines. Concurrently, legislation-driven changes have occurred in the composition of diesel fuel and design of the injection system of diesel engines. In the last decade, the introduction of ultra-low sulfur diesel (ULSD) and biodiesels, such as Fatty Acid Methyl Ester (FAME), have sought to improve the fuel side. The diesel injectors have seen combustion shaping, and an increase in temperature, pressure and the internal tolerance afforded to moving parts to fulfil the demands of emission legislation. Since these changes in fuels and diesel injectors, problems arising from deposit formation inside the injector have been reported worldwide, and form the subject of many studies with the aim of understanding and mitigating their negative effects.[32–35] This is a new topic and should not be confused with External Diesel Injector Deposits (EDIDs), which have some aspects of their formation which may transferred, but in general the formation of IDIDs takes place under different conditions.[36,37] The deposit and tighter internal injector restrictions have manifested into a problem for consumers as typically needles with deposits stick and stop the flow of diesel, hindering combustion and increasing emissions. IDIDs are of significant interest due to the detrimental effects on the consumer and environment. It is vital to understand the composition of the carbonaceous IDIDs to gain an insight into their formation mechanism. This information can then be applied to avoid their instigation and/or to design new additives to prevent formation or to aid in their removal. Due to the insoluble nature of the deposits and the small amounts of material available, analysis has been difficult.[7,29,30,32–35,38–40] In this study, we demonstrate the ability of HyPy to remove fluorescing species and thus facilitate μRS analysis of field sample IDIDs.

Experimental

Materials

General. The hydrogen and nitrogen gases used for pyrolysis were supplied by the British Oxygen Company (BOC) with a purity of 99.9%.

Reference samples. Details of the six carbon reference samples analysed by μRS are included in Table 1.

IDID samples. Details of the five IDIDs analysed by μRS analysis are included in Table 2. It is important to note that the

Table 1 Technical details of the reference carbon samples analysed by μRS in this study, including the commercial source or feedstock, the percentage of black or pyrolytic carbon in 8 ring or larger structures determined by HyPy (BC_{HyPy}), where applicable, and the percentage of total carbon

Reference carbon	Commercial source or feedstock	BC_{HyPy}/%	Total carbon/% dry ash free basis
Graphite	Sigma Aldrich (808067)	n/a	99
Multi-walled carbon nanotubes (MWCNT)	Sigma Aldrich (659258)	n/a	>90
Graphene oxide (GO)	William Blythe (JC05-163P)	n/a	68
Charcoal	Archaeological charcoal, neolithic age	24	52.7
Biochar-A	Whole tree wood Biochar	94	76.1
Biochar-B	Biochar from ancient coalified wood	97	92.4

Table 2 Technical details of the IDIDs analysed by μRS in this study, including the location where the engine component failed, the fuel used and the quoted complaint

IDID	Location	Fuel	Complaint
IDID-A	Norway	Diesel EN590	Injector needle from a heavy-duty truck. Complaints of a non-start due to needle sticking
IDID-B	Minnesota, USA	US No. 2 Diesel	Complaint of poor drivability
IDID-C	Louisiana, USA	US No. 2 Diesel	Complaints included power loss, and a workshop tow was required. The needle misfired after 40 min and stopped. There was no start
IDID-D	Norway	Diesel EN590	Injector needle from a heavy-duty truck. Complaints of a non-start due to needle sticking
IDID-E	China	China	Complaint of engine stopping

IDIDs were analysed by μRS whilst attached to the needle, *i.e.*, their removal was not required. The needles themselves contributed no significant signal in the Raman spectra. Details of the five IDIDs analysed by gas chromatography-mass spectrometry (GC-MS) are included in Table S8 of the SI.

Methods

Hydropyrolysis (HyPy). All the reference carbon and IDID samples were subject to HyPy. This process involved rapidly heating the sample to 250 °C (~50 °C min^{-1}), and then at a rate of 8 °C min^{-1} to 350 °C, under a hydrogen stream at 150 bar and a flow rate of 5 L min^{-1}. Once at 350 °C, the temperature was held for 5 min. The weights of the reference samples ranged between 10–35 mg. A silica trap and dry ice was used to isolate the volatile matter from the injector needles, which was subsequently analysed using GC-MS. The apparatus used for pyrolysis has been described in detail previously.[30,31,38,39]

Nitrogen pyrolysis (NPy). Select reference carbon and IDID samples were subject to NPy. This process involved rapidly heating the sample to 250 °C (~50 °C min^{-1}), and then at a rate of 8 °C min^{-1} to 350 °C, under a nitrogen stream at 150 bar and a flow rate of 5 L min^{-1}. Once at 350 °C, the temperature was held for 5 min. A silica trap and dry ice was used to isolate the volatiles.

Computed tomography (CT). One of the failed injector needles was scanned with a Pheonix V|tomex| M 240 X-ray CT system (GE Sensing and Inspection Technologies, GmbH, Wunsdorf, Germany) with a maximum electron acceleration voltage of 300 kV and detectable detail <1 μm. This analysis was performed to provide detailed, non-invasive macroscale imaging of the needle inside the injector body, without the need to remove it from the injector. Settings were as follows: 220 kV applied potential, 110 μA tube current, 29 μm resolution, 500 ms detector exposure time, 1800 radiograph images over 360° rotation, each radiograph was 1 image. The X-ray beam was filtered with 0.5 mm of copper. The total scan time was 25 min. The software used to analyse sample data was datos|x rec, and visualised using Volume Graphics VG StudioMax (Volume Graphics, GmbH, Heidelberg, Germany). It was not necessary to operate at maximum accelerating voltage as the spatial resolution required to visualise the failed needle was lower than the maximum achievable for this system.

Scanning electron microscopy (SEM). SEM analysis of one of the failed injector needles was performed using a XL30 FEG-ESEM (Thermo Fischer, Massachusetts, USA). The accelerating voltage used was 20 kV, with a spot size of 3.0 nm. The working distance was 28.2 mm. This analysis was performed to assess the microstructure of the IDID.

Gas chromatography mass spectrometry (GC-MS). GC-MS analysis of the thermally-labile products released from the injector needles following HyPy or NPy treatment was performed in full scan mode (m/z 40–400) using a 7890 GC gas chromatograph interfaced to a 5977 MSD mass spectrometer (Agilent, Santa Clara, USA). Separation was achieved on a HP-5MS fused silica capillary column (30 m × 250 μm × 0.25 μm), using helium as the carrier gas, and an oven programme involving heating to 50 °C, holding for 2 min, then heating to 300 °C at a rate of 4 °C min^{-1}, followed by final hold for 20.5 min. Samples were prepared for analysis by extracting the volatiles from silica using 10 mL dichloromethane, which were subsequently evaporated to 100 μL under a stream of nitrogen at room temperature prior to analysis.

Micro-Raman spectroscopy (μRS). μRS was performed using a LabRAM HR Raman microscope (HORIBA, Lille, France). Details of the range of instrument configurations applied in this study are included in Table 3.

Table 3 Technical details of the instrument configurations used for μRS measurements

Laser wavelength/nm	Laser power/mW [a]	Diffraction grating groove density/lines per mm	Objective lens magnification (numerical aperture)	Spectral resolution/cm^{-1} [b]	Lateral resolution/nm [c]
325	0.30	1200	40× (0.50)	2.5	—[d]
532	0.40	600	100× (0.80)	1.8	480
660	0.25	600	100× (0.80)	1.2	592
785	0.40	300	100× (0.75)	1.7	1070

[a] Measured at the sample using a power meter. [b] Defined as single pixel dispersion at the low-energy cut-off of the edge filter. [c] Estimated using a spatial resolution standard comprising 100 nm-wide gold stripes on silicon. [d] Not measured.

In all cases, the size of the confocal aperture was set to 200 μm. Prior to spectrum acquisition, the spectrometer was calibrated (for Raman shift) by application of an automated calibration procedure using the zero-order line (*i.e.*, the zeroth-order diffraction of incident laser light at 0 nm) and the phonon mode at 520.7 cm^{-1} from a Si (100) reference sample. Samples were prepared for analysis by casting powders onto Si. Spectra were acquired with 60 s integration time and 2 accumulations to remove spectral artefacts, *e.g.*, cosmic rays, and improve the signal-to-noise ratio, from a minimum of 3–5 random locations to enable investigation of sample heterogeneity. Where photobleaching was applied, specific details are included in the respective figure/table captions. Before spectra were processed, a measure of the baseline intensity (defined as I_{base}, in counts per s) was determined by extracting the intensity at 1900 cm^{-1}. Unless stated otherwise, spectra were processed using Labspec 6.7 software as follows: (i) extraction within the range 900–2000 cm^{-1}, (ii) baseline correction using a first-order polynomial function (64 anchor points, 16 noise points), (iii) normalisation to the intensity of the G band, and (iv) extraction of key peak parameters using the peak limits method. In this method, the height (maximum intensity value), area (maximum intensity value multiplied by the peak width), position (spectral position of the maximum intensity pixel) and width (approximate full-width at half-maximum of the peak) within a specified spectral range (*i.e.*, the "peak limits") can be extracted. Here, it was applied for determination of the position, width and intensity ratio ($I_D : I_G$ using peak heights) of the diagnostic D and G bands using the limits of 900–1500 and 1500–1900 cm^{-1} for the D and G bands, respectively. It is important to note that application of a linear baseline subtraction model and/or use of alternative numbers of anchor points (the number of data points used to fit the baseline) or noise points (a correction applied to the baseline calculation) have negligible impact on the ability to extract quantitative information from the spectra. OriginLab 10.2 software was employed for additional peak fitting analysis using Lorenzian lineshapes (three for graphite and MWCNT, four for GO, and five for charcoal, the Biochars and IDIDs). In all cases, the peak fitting was repeated until convergence was achieved, such that a chi-squared tolerance value of 1×10^{-6} was obtained. The same key peak parameters were extracted from the peak fits.

Results and discussion

The effect of HyPy and NPy on the structure of the reference samples

To assess the ability of HyPy and NPy to suppress fluorescence without impacting the fundamental structure of the carbon under examination, six reference carbons were initially explored, namely graphite, multi-walled carbon nanotubes (MWCNT), graphene oxide (GO), charcoal and two Biochars (Biochar-A and Biochar-B). These references were selected because they encompass a range of structural orders, with varying BC_{HyPy} contents and potential extents of baseline fluorescence. Graphite and MWCNT have low structural disorder, *i.e.*, exhibit little deviation from the ideal honeycomb lattice of sp^2-hybridised carbons expected in graphitic materials. Consequently, the first-order Raman spectrum of both graphite and MWCNT (Fig. 1) are dominated by a narrow, intense peak at ~1580 cm^{-1}, assigned as a C–C stretching vibration of

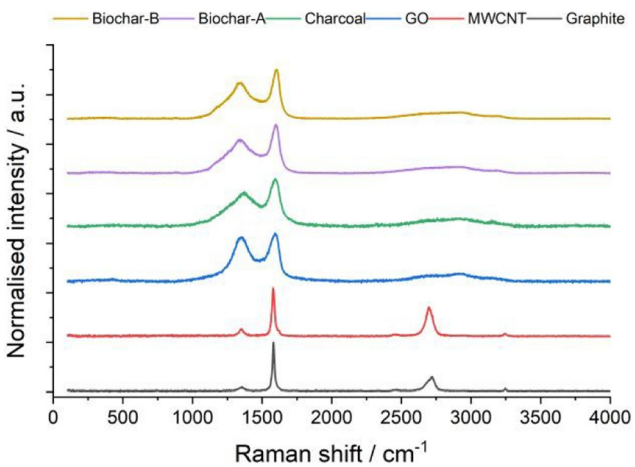

Fig. 1 Representative full Raman spectra (λ = 532 nm) of the six carbon reference samples employed in this study: graphite (black, bottom), MWCNT (red), GO (blue), charcoal (green), and Biochar-A (purple) and Biochar-B (yellow, top). Prior to spectrum acquisition, GO was photobleached for 100 s at P = 0.4 mW. The first-order Raman spectrum shows the characteristic D and G bands. The second-order Raman spectrum of ordered carbons, such as graphite and MWCNT, is dominated by the 2D band. In more disordered carbons, the intensity of the 2D band is reduced, with the second-order spectrum representing a superposition of several low-intensity overtone and combination modes, including the 2D, D + D′ and 2D′ bands.

E_{2g} symmetry (the so-called G "graphite" band), in addition to a similarly narrow but lower intensity peak at ~1350 cm^{-1}, an A_{1g} ring-breathing mode of six-atom rings requiring a defect for its activation (the so-called D "disorder" band), with often negligible contributions to the baseline intensity from fluorescence. Under the amorphisation trajectory defined by Ferrari and Robertson[11] such carbons would be classified as early stage 1. Conversely, charcoal and the Biochars are more disordered, exemplified by broader and more strongly overlapping D and G bands observed in the first-order Raman spectrum (Fig. 1) and typically more evident baseline fluorescence (Table 4). Whilst the origin of this fluorescence is not fully understood, it is likely associated with HOMO–LUMO transitions in polycyclic aromatic hydrocarbons (PAHs) and/or functionalised alkenes, *i.e.*, species containing sp^2-hybridised carbons, either inherent to, or a byproduct within, the carbon itself.[41,42] Such carbons are considered early-to-mid stage 2 according to the amorphisation trajectory. GO – a solution-processable proxy for graphene with highly tuneable properties related to its high, but variable, oxygenated functional group content, and currently finding broad-spectrum applications including in biomedicines, water treatment and composites[43,44] – is similarly disordered, presenting a Raman spectrum (Fig. 1) similar to that of the charcoal and the two Biochars. However, its analysis by μRS is hindered by often significant, sometimes dominant, baseline fluorescence, attributed to electron–hole recombination from the bottom of the conduction band and nearby localised states to a wide-range valence band, involving both non-oxidised carbon atom regions and the boundary of oxidised carbon atoms, *e.g.*, in C–O, C═O and –(C═O)OH functional groups.[44] It is worthy of note that GO does not readily map onto the amorphisation trajectory owing to the presence of oxygen-containing functional groups not considered within the ternary phase diagram of carbon.

Whilst the positions, widths and lineshapes of the D and G bands provide key information on the physicochemical attributes of carbons, *e.g.*, extents of strain, doping, *etc.*, it is the intensity ratio of D and G bands ($I_D : I_G$) that is most used for quantification of ordering with graphitic carbons.[45] However, interpretation of this simple metric is fraught with errors throughout the wider scientific literature and worthy of brief discussion.[46,47] Firstly, carbons are known to possess high sensitivity to excitation laser power. Indeed, in control measurements of our reference samples (Fig. S1–S6, SI) we found that analysis at laser powers above 0.4 mW resulted in changes in $I_D : I_G$ as a direct result of laser-induced heating. The use of appropriate laser powers, typically $P < 0.5$ mW for substrate-bound carbons, is therefore critical to prohibit the onset of photothermal transformations. Secondly, owing to the double-resonance scattering mechanism and consequential dispersive nature of the D band,[48,49] its position and intensity shows strong wavelength dependence (Fig. S7–S13 and Table S1, SI). As such, meaningful comparisons of $I_D : I_G$ can only be made by considering spectra collected using the same excitation laser wavelength, and ideally the instrument configuration[45] as even changes in hardware, such as diffraction grating groove density, can impact $I_D : I_G$. Lastly, the relationship between $I_D : I_G$ and defect density (*cf.* interdefect distance, L_D) is complex. At low defect density, the development of a D peak (increasing $I_D : I_G$) indicates increasing *disorder* (*i.e.*, the likelihood of locating any defect, as this ring-breathing mode cannot be activated in the absence of a defect) with $I_D : I_G \sim 1/L_D$ according to the Tuinstra and Koenig relationship.[50] For more disordered carbons, the development of a D peak indicates increasing *order* (*i.e.*, the probability of observing a six-atom ring) and consequently is better described as $I_D : I_G \sim {L_D}^2$ consistent with the model developed by Ferrari and Robertson.[11] Therefore, caution must be exercised when attempting to extract physical meaning from $I_D : I_G$.

Visual inspection and subsequent analysis of the 532 nm Raman spectra obtained from the six reference carbons (Fig. 1 and Table 4) confirm the expected range of structural orders,

Table 4 Spectral characteristics extracted using the peak limits method from the point spectra (λ = 532 nm) of the reference carbons investigated in this study by μRS before treatment and after HyPy. Values are quoted as mean plus/minus one standard deviation from N = 5 measurements. Application of the peak limits method was deemed more appropriate than peak fitting as the inability to reliably deconvolute the G and D′ bands through fitting significantly impacted the determined $I_D : I_G$ (*cf.* von Neumann's maxim)

			D band		G band		
Reference carbon	Treatment	I_{base}/counts per s	Position/cm^{-1}	Width/cm^{-1}	Position/cm^{-1}	Width/cm^{-1}	$I_D : I_G$
Graphite	None	1.8 ± 0.1	1351.9 ± 2.6	52.0 ± 3.7	1581.3 ± 1.3	21.4 ± 2.5	0.17 ± 0.07
	HyPy	1.3 ± 0.1	1350.3 ± 6.7	54.5 ± 3.5	1579.7 ± 0.7	19.8 ± 4.2	0.15 ± 0.09
MWCNT	None	1.6 ± 0.1	1350.3 ± 2.6	45.6 ± 7.3	1579.4 ± 1.5	23.3 ± 1.5	0.14 ± 0.03
	HyPy	1.2 ± 0.0	1352.5 ± 2.4	42.4 ± 1.8	1580.7 ± 3.0	23.6 ± 1.3	0.14 ± 0.03
GO	None[a]	92.6 ± 49.3	1348.0 ± 10.0	163.0 ± 14.2	1593.1 ± 3.2	103.5 ± 6.5	0.93 ± 0.03
	HyPy	6.9 ± 1.7	1354.1 ± 5.1	158.6 ± 5.0	1593.4 ± 4.2	93.6 ± 2.1	0.90 ± 0.01
Charcoal	None	311.8 ± 106.5	1367.8 ± 6.5	269.1 ± 11.7	1598.0 ± 3.6	123.1 ± 15.1	0.77 ± 0.07
	HyPy	187.9 ± 69.8	1365.2 ± 6.6	223.3 ± 4.6	1601.7 ± 1.8	58.5 ± 2.0	0.59 ± 0.01
Biochar-A	None	33.0 ± 29.3	1338.8 ± 7.6	274.6 ± 2.7	1599.2 ± 3.5	84.8 ± 4.7	0.73 ± 0.02
	HyPy	10.7 ± 2.2	1341.0 ± 4.0	274.0 ± 2.4	1598.3 ± 3.4	86.4 ± 2.8	0.74 ± 0.01
Biochar-B	None	17.1 ± 11.3	1339.8 ± 6.8	236.1 ± 16.7	1603.7 ± 2.3	76.1 ± 1.3	0.73 ± 0.04
	HyPy	6.2 ± 2.1	1333.5 ± 4.3	216.8 ± 16.4	1602.7 ± 2.2	74.9 ± 1.8	0.75 ± 0.03

[a] Prior to spectrum acquisition, GO not subject to thermal treatment (*i.e.*, before) was photobleached for 100 s at P = 0.4 mW.

exemplified by the $I_D : I_G$ values observed (0.14–0.93). Moreover, it was noted that acquisition of the Raman spectrum of GO, and to a lesser extent charcoal, was complicated by fluorescence. As discussed previously, there are various reported methods for fluorescence suppression, including changing the wavelength of the excitation laser and photobleaching. To explore the potential of these methods here, the reference carbons were analysed using a range of excitation wavelengths, spanning the UV-visible-NIR range (Fig. S7–S13 and Table S1, SI), and separately subject to higher power, short duration (Fig. S14–S19, SI) and low power, longer duration photobleaching approaches (Fig. S20–S25, SI). In all cases, to quantify the baseline intensity, which will inevitably be higher where fluorescence is observed, we introduced and used a new metric – I_{base} – defined as the intensity of the baseline in counts per s at 1900 cm^{-1}, *i.e.*, near to, but not overlapping with, the D or G bands. For more ordered carbons, where I_{base} was low at λ = 532 nm (<2 counts per s, *i.e.*, a measure of the system noise) and fluorescence not an issue, changing the wavelength of the excitation laser had negligible impact (Fig. S7, S8 and S13 and Table S1, SI). However, for more disordered carbons where I_{base} at λ = 532 nm was more significant, a strong wavelength-dependence was observed, with I_{base} seemingly increasing with increasing laser wavelength (Fig. S9–S13 and Table S1, SI). In fact, for GO and charcoal it was not possible to record a 785 nm Raman spectrum owing to the dominance of fluorescence at this wavelength resulting in detector saturation. The application of higher power, short duration photobleaching, whilst to an extent remedying the fluorescence issue (*i.e.*, reducing I_{base}), is not an appropriate solution owing to the irreversible structural and power-dependent changes to the carbon induced at high laser power (P > 0.4 mW) (Fig. S14–S19, SI). Interestingly, low power (P < 0.4 mW), longer duration photobleaching was, overall, an effective tool for fluorescence suppression. Through acquisition of time maps, where a series of Raman spectra were collected over the course of 5 minutes (Fig. S20–S25, SI), we found that: (i) in all cases, the spectra obtained towards the end of the time map were analogous to those obtained nearer the start, *i.e.*, low power photobleaching does not seemingly impact the structure of the carbon; (ii) for ordered carbons, there was no strong dependence on I_{base} with either time or laser wavelength, *i.e.*, the baseline intensity was stable; and (iii) for GO, and to a lesser extent charcoal, I_{base} could be effectively reduced to a level where meaningful Raman spectra could be obtained by photobleaching at P < 0.4 mW, regardless of the wavelength of the laser applied. However, it is important to note that photobleaching was not universally applicable as increases in baseline intensity with extended bleaching was observed in some cases.

Given that instrument-based solutions for fluorescence suppression could not seemingly be applied ubiquitously, HyPy was next explored and a qualitative inspection of the Raman spectra obtained from post-HyPy carbons relative to the parent (untreated) carbons undertaken (Fig. 2).

Careful examination of the spectral profiles, including extraction of key peak attributes using either the peak limit (Table 4 and Fig. 3) or peak fitting methods (Fig. S26–S31 and Table S2, SI), indicates that HyPy has no significant impact on the structure of the carbons, with negligible changes in the positions, widths and intensity ratios of the D and G bands (within the standard deviation of N = 5 measurements) observed for the majority of the reference carbons. Moreover, examination of I_{base} reveals that HyPy effectively reduces the baseline intensity associated with fluorescence. The most significant fluorescence suppression was noted for GO, where I_{base} was reduced to ~7 counts per s following HyPy, from ~900 counts per s for the parent carbon in the absence of photobleaching (~90 counts per s after 100 seconds of low-power photobleaching), *i.e.*, HyPy reduces the baseline fluorescence intensity by up to two orders of magnitude compared to photobleaching reducing it by approximately one order of magnitude. The exception here was charcoal where more evident changes in the spectral profile, and indeed $I_D : I_G$, and only moderate reductions in I_{base}, were observed following HyPy. This could arise from the relatively low BC_{HyPy} content (Table 1) and residual amounts of labile material remaining after HyPy.

To briefly explore the impact of pyrolysis under different conditions, a subset of the reference samples was treated using HyPy at higher temperatures (Fig. S32 and Table S3, SI) and separately using NPy (Fig. S33–S36 and Table S4, SI). Interestingly, HyPy treatment of Biochar-A at 550 °C resulted in a small decrease in $I_D : I_G$ and subtle narrowing of both the D and G bands, in addition to a negligible reduction in I_{base} relative to the parent, indicating that HyPy should likely be applied at a maximum temperature of 350 °C in order to preserve the structural integrity of the carbon whilst remediating the fluorescence issue. The success of treatment of graphite, GO and Biochar-A using NPy was more variable. In general, I_{base} was reduced and $I_D : I_G$ unaffected, consistent with the results observed using HyPy, but for GO the width of the D band increased significantly (from ~160 to ~240 cm^{-1}), indicating an increase in the range, but not number, of defects present, likely a result of nitrogen-doping. Whilst there is inevitably more parameter space that can be explored, HyPy at 350 °C was found to be effective for fluorescence suppression and as such suitable for application to trickier samples, *e.g.*, engine-derived carbons, where fluorescence will be more significant.

The application of HyPy and NPy to IDIDs

As discussed previously,[51] IDIDs are commonly found to develop on the injector needle and tip due to the high temperature and pressure conditions found in these regions that promote the pyrolysis of fuel and polymerisation reaction and result in sticky carbonaceous deposits. Indeed, our photography and SEM analysis of a representative failed injector shows a clear carbonaceous deposit at the tip of the needle (Fig. 4).

As anticipated, Raman spectroscopy analysis of the IDIDs at λ = 532 nm was significantly impacted by fluorescence (Fig. S37–S42 and Table S5, SI), with I_{base} highly variable location-to-location and on average typically more than 1000

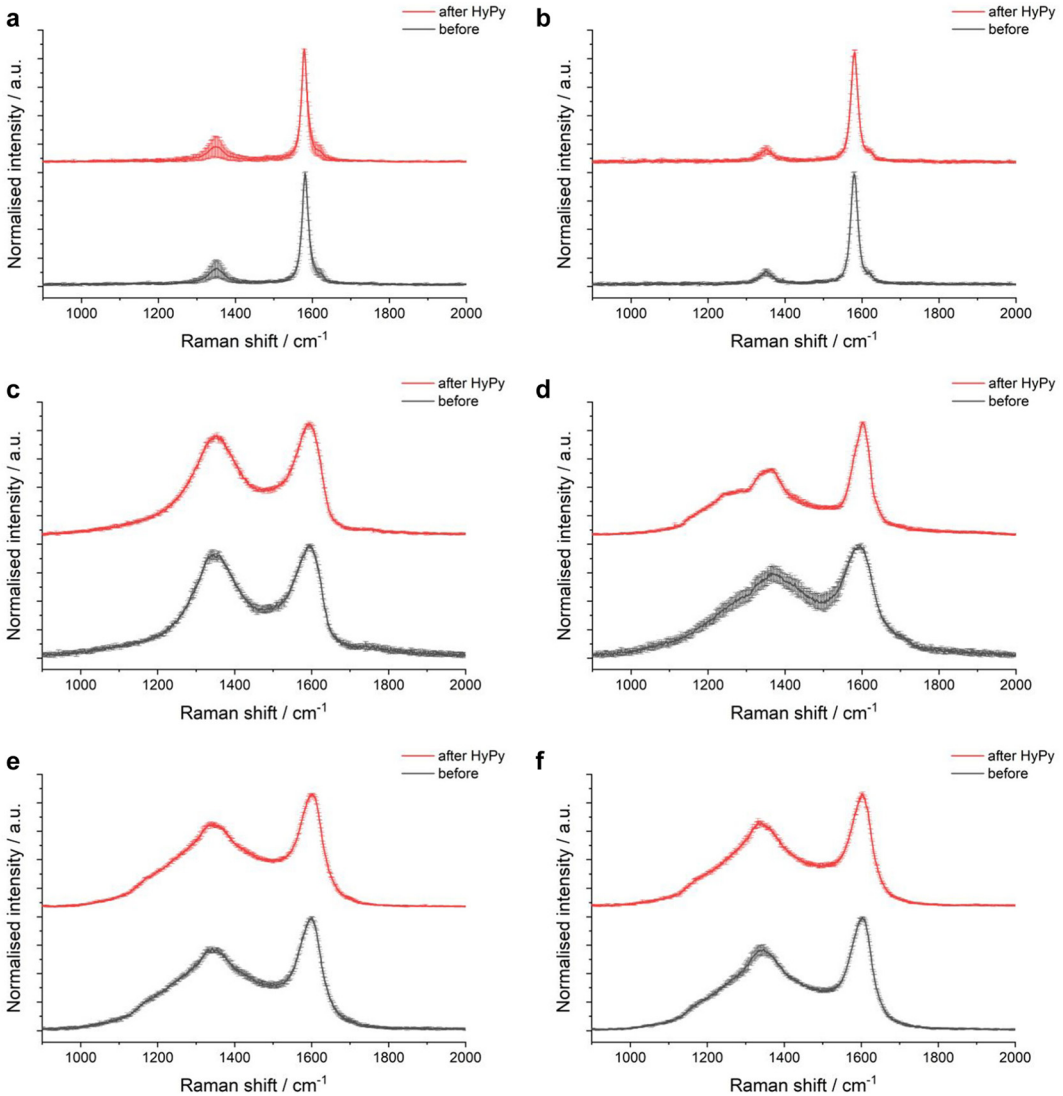

Fig. 2 Mean Raman spectra (λ = 532 nm) of (a) graphite, (b) MWCNT, (c) GO, (d) charcoal, (e) Biochar-A and (f) Biochar-B before (black, bottom) and after HyPy (red, top). Error bars reflect one standard deviation from N = 5 measurements. Prior to spectrum acquisition, GO not subject to thermal treatment (*i.e.*, before) was photobleached for 100 s at P = 0.4 mW.

counts per s, well above the level for detector saturation and precluding acquisition of spectra. Multiple-wavelength and time-dependent analysis of IDID-A indicated that increasing the wavelength of the excitation laser generally increases I_{base}, as was seen for the more disordered reference carbons, with low power photobleaching failing to reduce the baseline fluorescence to the levels required for μRS. It is interesting to note that I_{base} for IDID-A at λ = 325 nm was low enough, following an extended period of photobleaching, for Raman spectra to be obtained. This enabled us to confirm the innocence of HyPy (and NPy) for IDIDs (Fig. S43 and Table S6, SI). However, it is worth reiterating that most modern Raman systems are not equipped with UV laser excitation sources, with changes in $I_D : I_G$ harder to discern using shorter wavelength lasers owing to the dispersive nature of the D band, and therefore HyPy might represent a more generally applicable tool for fluorescence suppression than photobleaching and subsequent analysis with UV lasers.

Indeed, following HyPy treatment the 532 nm Raman spectra of the IDIDs could be readily acquired (Fig. 5 and Table 5). It is important to note that it was not possible to obtain 532 nm Raman spectra of the IDIDs following NPy (Fig. S44, SI) as, even following extensive, low power photobleaching, which in some locations increased the fluorescence baseline, I_{base} remained too high. This can be explained by the inability of nitrogen to remove carbon–carbon double bonds, as is seen with HyPy.

Analysis of I_{base} shows that the baseline intensity can be reduced by more than an order of magnitude relative to the parent carbon through application of HyPy and thus enabling 532 nm Raman spectra of the IDIDs to be collected and analysed. Overall, the spectra observed are consistent with those

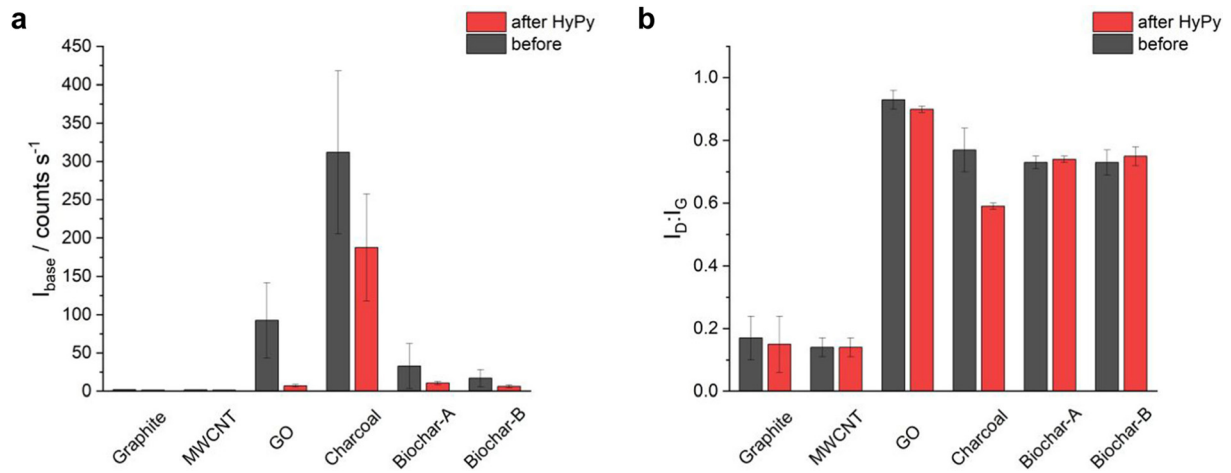

Fig. 3 (a) I_{base} and (b) $I_D : I_G$ before treatment (black) and after HyPy (red) for the reference carbons investigated in this study. Error bars reflect one standard deviation from $N = 5$ measurements. Prior to spectrum acquisition, GO not subject to thermal treatment (*i.e.,* before) was photobleached for 100 s at $P = 0.4$ mW.

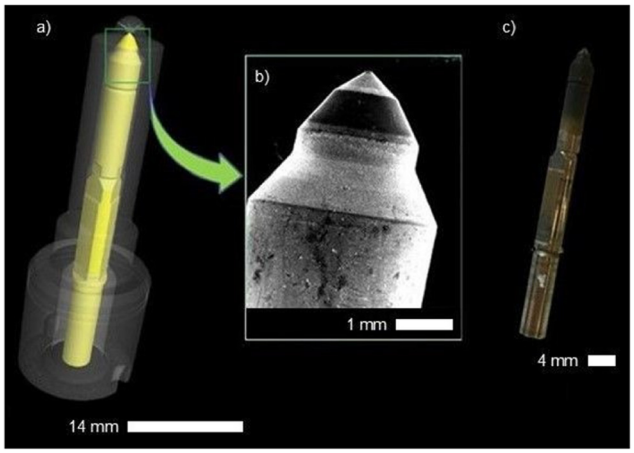

Fig. 4 Multiple length scale imaging of a typical injector needle. (a) A CT image of a needle inside the injector, prior to its removal from the injector body for subsequent analyses. (b) A SEM image (61× magnification) showing the surface morphology of the injector needle and the discontinuous IDID coverage responsible for the needle sticking. (c) A photograph of a failed needle removed from the injector body, covered in carbonaceous material at the tip, appearing as black matter.

obtained from the reference carbons GO, charcoal and the Biochars, comprising two broad and strongly overlapping D and G bands, indicating disorder but on a journey towards a more ordered carbon phase. Examination of the spectral profiles, through both the peak limit (Fig. 5 and Table 5) and peak fitting methods (Fig. S45–S49 and Table S7, SI), indicates that IDID-C is seemingly the least impacted by baseline fluorescence (lowest I_{base}), and the most ordered (narrowest D and G bands and highest $I_D : I_G$), consistent with a carbon that would be highly challenging to remove from the injector and explains the failure observed. It is important to note that the IDID needles used in the study are from "field" issues and as such have seen a wide variety of fuels, conditions, injector settings, field age, and driving range, all of which adds to IDID accumulation until it has noticeable impact on engine performance. Such variability explains the spectral differences observed and echoes the build-up of ring structure seen in previous studies on fuel deposits. The degree of movement towards ordered carbonaceous deposits is indicative of the mechanism of IDID formation and a combination of μRS and HyPy are well placed to deliver this important data.[52,53]

Identification of contaminant volatile species

GC-MS was used to analyse the volatile material released during pyrolysis *via* HyPy and NPy up to 350 °C from a complementary set of IDIDs and help identify the species responsible for the fluorescence interference observed in the Raman spectra (Fig. 6 and Table S8, SI). Both the total ion chromatogram (TIC) and the m/z 71 single ion chromatogram (SIC) arising from acyclic alkanes which help to identify the major alkane species are shown. As the volatile products from each needle were dissolved in an equal volume of solvent prior to analysis, this confirms that considerably less volatile material was removed under NPy conditions than with HyPy, consistent with the observations from μRS. *n*-Hexadecane and *n*-octadecane were not major constituents in the NPy products, due a combination of cracking and rearrangement reactions and, clearly, NPy is not effective at reducing the unsaturated species derived from biodiesel that are responsible for the fluorescence.

The HyPy products from needles F–H all comprise *n*-hexadecane, *n*-octadecane, together with other *n*-alkanes (C_{12}–C_{26}) (Fig. 6). Diesel fuel is the likely origin of the C_{12}–C_{26} *n*-alkanes, giving a reasonably equal distribution and intensity of peaks, seen in many examples in previous studies.[54] The relatively high levels of *n*-hexadecane and *n*-octadecane arise from the methyl esters in biodiesel incorporated into the deposits.

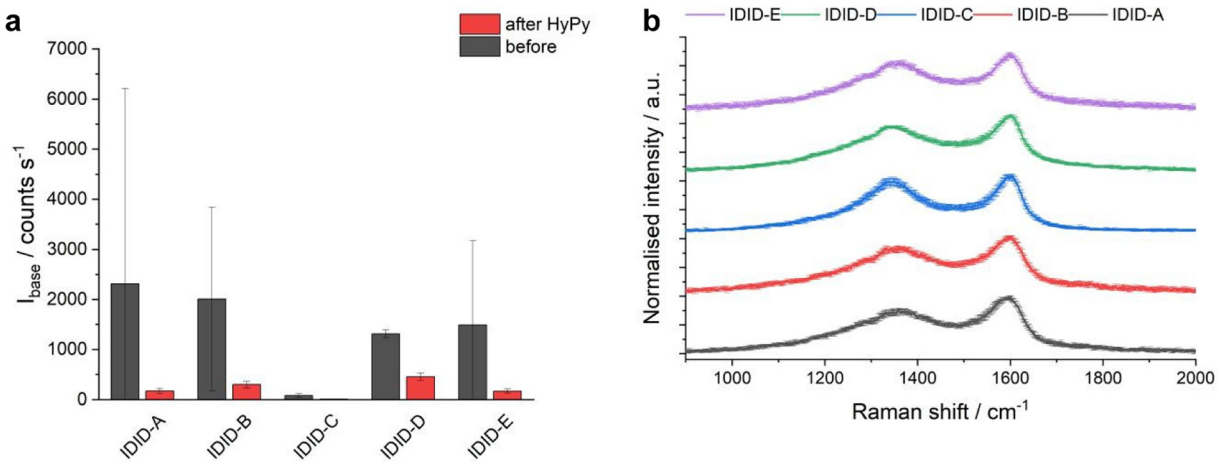

Fig. 5 (a) I_{base} and (b) mean Raman spectra (λ = 532 nm) of the IDIDs after HyPy. Error bars reflect one standard deviation from N = 5 measurements. Prior to spectrum acquisition and extraction of I_{base} in (a), IDIDs not subject to thermal treatment (*i.e.*, before) were photobleached for 300 s at P = 0.4 mW.

Table 5 Spectral characteristics extracted using the peak limits method from the point spectra (λ = 532 nm) of the IDIDs after HyPy treatment investigated in this study by μRS. Values are quoted as mean plus/minus one standard deviation from N = 5 measurements

		D band		G band		
IDID	I_{base}/counts per s	Position/cm^{-1}	Width/cm^{-1}	Position/cm^{-1}	Width/cm^{-1}	$I_D : I_G$
IDID-A	176.2 ± 47.6	1360.2 ± 11.5	256.2 ± 6.4	1591.6 ± 9.8	121.6 ± 13.8	0.77 ± 0.03
IDID-B	296.4 ± 59.0	1344.9 ± 18.4	247.5 ± 3.1	1598.1 ± 3.1	127.2 ± 6.4	0.82 ± 0.02
IDID-C	12.5 ± 4.6	1340.8 ± 7.3	178.5 ± 29.2	1600.0 ± 4.8	91.4 ± 12.3	0.91 ± 0.07
IDID-D	452.1 ± 70.6	1342.4 ± 10.6	269.8 ± 4.9	1600.9 ± 1.3	118.2 ± 16.0	0.81 ± 0.01
IDID-E	172.5 ± 39.0	1365.6 ± 12.9	250.4 ± 7.4	1600.0 ± 2.8	115.3 ± 8.9	0.87 ± 0.02

There is also the possibility that lubricity and corrosion inhibition additives, albeit present in ppm concentrations, also containing functionalised n-C_{16} and n-C_{18} acids, could contribute to the n-hexadecane and n-octadecane observed. Thus, the fluorescence probably arises from unsaturated n-C_{16} and n-C_{18} chains from biodiesel that are fully reduced during HyPy.[55] Needle G was ran on ULSD, with unknown additives present in the fuel; however, due to the lubricity properties of ULSD, it is likely there would have been an additive package. The GC-MS data shows a large distribution of high molecular weight species mostly above n-C_{18}. Needle H was obtained from a DW10B engine test ran on RF06 reference fuel with no additives but with added non-commercial low molecular weight polyisobutylene succinimide (PIBSI), which has been known to cause sticking.[35]

Needle I displays a uniform distribution of n-alkanes in the range C_{12}–C_{26} and, as with needles F–H, these were likely derived from a diesel fuel as needle I was run on a ULSD. The chromatogram for the alkanes in needle J is dominated by an unresolved complex mixture (UCM) where the branched alkanes, which could arise from lube oil. Furthermore, a series of doublets in the TIC is evident, identified as isomers arising from methyl-substituted alkenes based on nonene, which could be derived from the PIBSI present in this fuel. These peaks are not observed for Needle G in HyPy because the PIBSI chains are not subjected to extensive cracking as in NPy.

Mechanistic considerations

Overall, the evidence supports the building of archipelago ring structures.[29,52] In IDID formation, a reversal of the amorphisation trajectory described by Ferrari[11] from fuel to ordered carbon occurs, as depicted in Fig. 7. In stage 3, the change in carbon atom hybridisation from sp^3 to sp^2 represents the onset of aromatisation, whilst, in stage 2, aromatic structures increase in ring size, increasing the intensity of the G band. At stage 1, the G band moves from ~1580 to 1600 cm^{-1} with chains of sp^2-hybridised carbon atoms converting into large ring structures, the D band reducing as there is a reduction of the topological disorder within an ordered graphitic layer.[56] Clearly, the needles analysed are nearer to stage 1 than 3 because of the processing whereby small ring aromatic structures will have been released as volatiles in HyPy.[30] For NPy, the possible formation of aryl nitrogen species cannot be ruled out. However, as noted by Ferrari,[56] there is little difference in the D–G region due to nitrogen-containing and nitrogen-free carbon films, so the NPy spectra can be compared with their HyPy counterparts. The fact that G bands are observed at

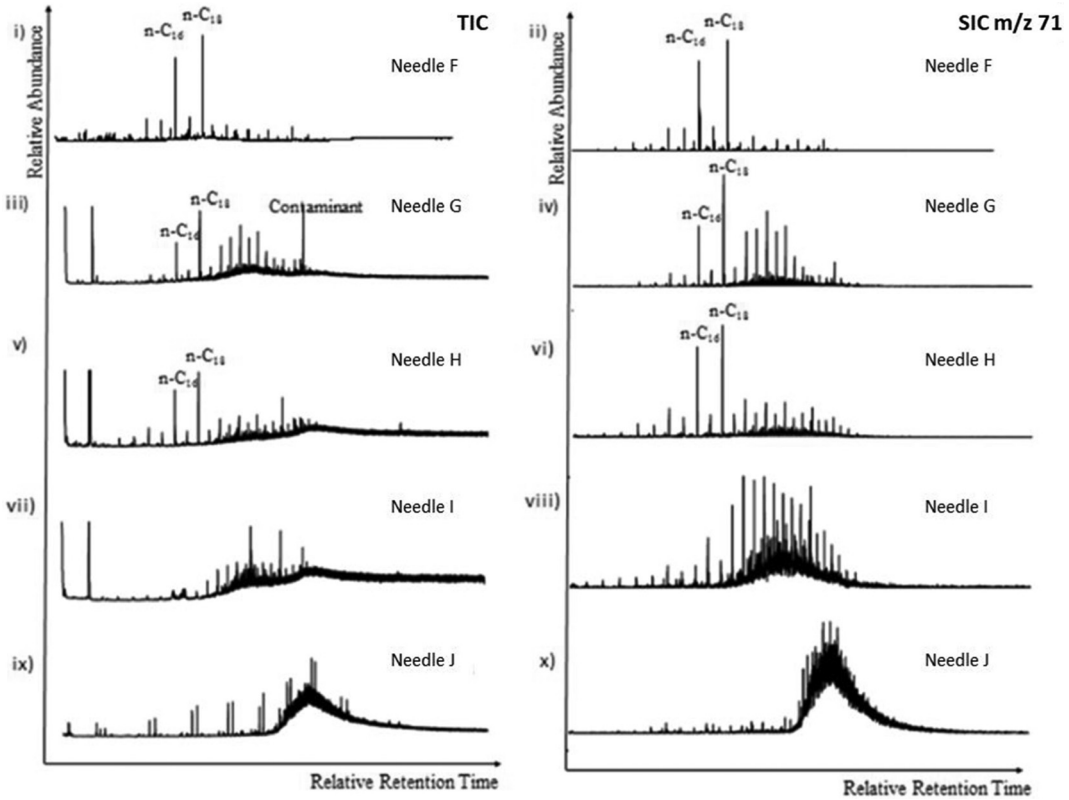

Fig. 6 Total ion chromatogram (TIC) and single ion chromatogram (SIC) *m/z* 71 of volatiles released from needles F–H in HyPy and needles I–J in NPy. *n*-C_{16} = hexadecane; *n*-C_{18} = octdecane.

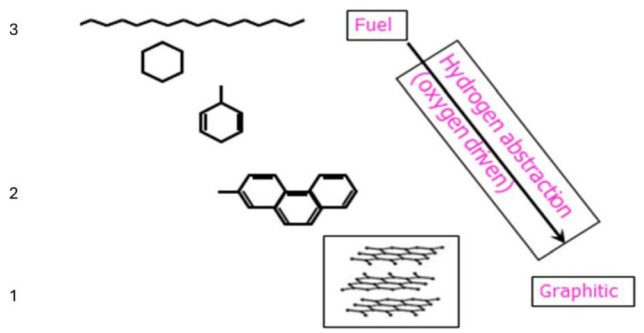

Fig. 7 Amorphisation trajectory from fuel to ordered carbon with the stage numbers described by Ferrari.[11]

higher Raman shift for the NPy residues could reflect the additional aromatisation that has occurred compared to HyPy.

Conclusions

We have shown that HyPy successfully removes the fluorescing species from carbonaceous deposits in IDIDs to facilitate first-time characterisation by μRS. Systematic analysis of six carbonaceous reference materials, spanning a range of structural orders, carbon contents and extent of fluorescence, demonstrates a considerable reduction in baseline intensity but with negligible changes in $I_D : I_G$ following HyPy. This is most clearly observed for GO, a technologically-important carbon-based material which can be challenging to analyse by μRS, with HyPy treatment surpassing the results observed using the more commonly explored options of alternative excitation laser wavelengths and/or photobleaching. NPy has similarly minimal impact on $I_D : I_G$, but there is some evidence for a change in the range of defects within the carbon and is therefore less desirable. For the IDID carbonaceous deposits, GC-MS analysis of the volatile species released following HyPy indicates that the fluorescence arises from unsaturated *n*-C_{16} and *n*-C_{18} fuel components. The profiles obtained from μRS analysis of the IDIDs are similar to those acquired from the more disordered reference carbons. Hydropyrolysis can be applied to a variety of other carbonaceous samples, including petroleum source rocks and shales, where fluorescence is likely to arise from additives in the drilling muds.

Author contributions

Joel Viggars: investigation, funding acquisition, writing – review & editing. Sarah Angel-Smith: investigation, funding acquisition, writing – original draft. Graham A. Rance: formal analysis, investigation, writing – review & editing. Ahmed Khairy: investigation. Will Meredith: investigation, writing –

original draft, writing – review & editing. Adrienne Davies: investigation. Jim Barker: conceptualization, funding acquisition, supervision, writing – original draft, writing – review & editing. Jaqueline Reid: investigation, writing – original draft. David J. Scurr: conceptualization, funding acquisition, supervision, writing – original draft, writing – review & editing. Colin E. Snape: conceptualization, funding acquisition, supervision, writing – original draft, writing – review & editing.

Conflicts of interest

There are no conflicts of interest to declare.

Data availability

The authors confirm that the data supporting the findings of this study are available within the article and its supplementary information (SI). Supplementary information, including additional μRS analysis, is available. See DOI: https://doi.org/10.1039/d5an00347d.

Acknowledgements

This research has been funded by Innospec Ltd and the Engineering and Physical Science Research Council (EPSRC), as part of the Centre of Doctoral Training in Efficient Fossil Energy Technologies at the University of Nottingham (EP/L016362/1) and the Centre for Resilient Decarbonised Fuel Energy Systems (EP/S022996/1). The authors are grateful to the Nanoscale and Microscale Research Centre (nmRC) for providing access to Raman spectroscopy facilities.

References

1 C. Cardell and I. Guerra, An overview of emerging hyphenated SEM-EDX and Raman spectroscopy systems: Applications in life, environmental and materials sciences, *TrAC, Trends Anal. Chem.*, 2016, **77**, 156–166, DOI: 10.1016/J.TRAC.2015.12.001.

2 A. Hédoux, Recent developments in the Raman and infrared investigations of amorphous pharmaceuticals and protein formulations: A review, *Adv. Drug Delivery Rev.*, 2016, **100**, 133–146, DOI: 10.1016/j.addr.2015.11.021.

3 S. V. Goryainov, Y. Pan, M. B. Smirnov, W. Sun and J. X. Mi, Raman investigation on the behavior of parasibirskite CaHBO3 at high pressure, *Spectrochim. Acta, Part A*, 2017, **173**, 46–52, DOI: 10.1016/J.SAA.2016.08.040.

4 H. M. Mohamed, Green, environment-friendly, analytical tools give insights in pharmaceuticals and cosmetics analysis, *TrAC, Trends Anal. Chem.*, 2015, **66**, 176–192, DOI: 10.1016/J.TRAC.2014.11.010.

5 W. Ji, B. Zhao and Y. Ozaki, Semiconductor materials in analytical applications of surface-enhanced Raman scattering, *J. Raman Spectrosc.*, 2016, **47**(1), 51–58, DOI: 10.1002/JRS.4854.

6 L. Bokobza, J. L. Bruneel and M. Couzi, Raman spectroscopy as a tool for the analysis of carbon-based materials (highly oriented pyrolitic graphite, multilayer graphene and multiwall carbon nanotubes) and of some of their elastomeric composites, *Vib. Spectrosc.*, 2014, **74**, 57–63, DOI: 10.1016/J.VIBSPEC.2014.07.009.

7 J. Barker, *et al.*, The characterisation of diesel internal injector deposits by focused ion-beam scanning electron microscopy (FIB-SEM), transmission electron microscopy (TEM), atomic force microscopy and Raman spectroscopy, *SAE [Tech. Pap.]*, 2015, DOI: 10.4271/2015-01-1826.

8 P. Charbonneau and J. S. Wallace, Scanning electron microscopy and Raman spectroscopy studies of ULSD and biodiesel soot loading in a diesel particulate filter, *SAE [Tech. Pap.]*, 2009, DOI: 10.4271/2009-01-1261.

9 A. C. Ferrari, Determination of bonding in diamond-like carbon by Raman spectroscopy, *Diam. Relat. Mater.*, 2002, **11**, 1053–1061, DOI: 10.1016/S0925-9635(01)00730-0.

10 A. C. Ferrari, Raman spectroscopy of graphene and graphite: Disorder, electron–phonon coupling, doping and nonadiabatic effects, *Solid State Commun.*, 2007, **143**(1–2), 47–57, DOI: 10.1016/J.SSC.2007.03.052.

11 A. C. Ferrari and J. Robertson, Interpretation of Raman spectra of disordered and amorphous carbon, *Phys. Rev. B*, 2000, **61**(20), 14095–14107, DOI: 10.1103/PhysRevB.61.14095.

12 J. G. Grasselli, M. K. Snavely and B. J. Bulkin, Applications of Raman spectroscopy, *Phys. Rep.*, 1980, **65**(4), 231–344, DOI: 10.1016/0370-1573(80)90065-4.

13 K. O. Lee, J. Zhu, S. Ciatti, A. Yozgatligil and M. Y. Choi, Sizes, graphitic structures and fractal geometry of light-duty diesel engine particulates, *SAE [Tech. Pap.]*, 2003, DOI: 10.4271/2003-01-3169.

14 S. Zhang, X. T. Zeng, H. Xie and P. Hing, A phenomenological approach for the Id/Ig ratio and sp3 fraction of magnetron sputtered a-C films, *Surf. Coat. Technol.*, 2000, **123**(2–3), 256–260, DOI: 10.1016/S0257-8972(99)00523-X.

15 P. Sathy, R. Philip, V. P. N. Nampoori and C. P. G. Vallabhan, Effect of a fluorescing impurity on the characteristics of stimulated Raman scattering from acetone, *Pramana*, 1992, **38**(6), 673–679, DOI: 10.1007/BF02875063.

16 G. N. Okolo, *et al.*, Chemical-structural properties of South African bituminous coals: Insights from wide angle XRD-carbon fraction analysis, ATR-FTIR, solid state ^{13}C NMR, and HRTEM techniques, *Fuel*, 2015, **158**, 779–792, DOI: 10.1016/J.FUEL.2015.06.027.

17 L. Lu, V. Sahajwalla, C. Kong and D. Harris, Quantitative X-ray diffraction analysis and its application to various coals, *Carbon*, 2001, **39**(12), 1821–1833, DOI: 10.1016/S0008-6223(00)00318-3.

18 M. Solum, A. Sarofim, R. Pugmire, T. Fletcher and H. Zhang, 13-C NMR analysis of soot produced from model compounds and a coal, 2001, Faculty Publications

Accessed: 01 Dec 2025 [Online]. Available: https://scholarsarchive.byu.edu/facpub/7044.

19 L. Jensen and G. C. Schatz, Resonance Raman scattering of Rhodamine 6G as calculated using time-dependent density functional theory, *J. Phys. Chem. A*, 2006, **110**(18), 5973–5977, DOI: 10.1021/JP0610867.

20 A. M. Saariaho, A. S. Jääskeläinen, P. Matousek, M. Towrie, A. W. Parker and T. Vuorinen, Resonance Raman spectroscopy of highly fluorescing lignin containing chemical pulps: Suppression of fluorescence with an optical Kerr gate, *Holzforschung*, 2004, **58**(1), 82–90, DOI: 10.1515/HF.2004.011.

21 R. M. El-Abassy, B. von der Kammer and A. Materny, UV Raman spectroscopy for the characterization of strongly fluorescing beverages, *LWT – Food Sci. Technol.*, 2015, **64**(1), 56–60, DOI: 10.1016/J.LWT.2015.05.026.

22 S. A. Asher, UV resonance Raman studies of molecular structure and dynamics: applications in physical and biophysical chemistry, *Annu. Rev. Phys. Chem.*, 1988, **39**, 537–588, DOI: 10.1146/annurev.pc.39.100188.002541.

23 S. A. Asher and C. R. Johnson, Raman spectroscopy of a coal liquid shows that fluorescence interference is minimized with ultraviolet excitation, *Science*, 1984, **225**(4659), 311–313, DOI: 10.1126/science.6740313.

24 S. P. A. Fodor, R. P. Rava, R. A. Copeland and T. G. Spiro, H2 Raman–shifted YAG laser ultraviolet Raman spectrometer operating at wavelengths down to 184 nm, *J. Raman Spectrosc.*, 1986, **17**(6), 471–475, DOI: 10.1002/jrs.1250170609.

25 S. M. Grayson, A Simple Visualization of Double Bond Properties: Chemical Reactivity and UV Fluorescence, *J. Chem. Educ.*, 2012, **89**(7), 925–927, DOI: 10.1021/ed200627c.

26 C. A. Lieber and A. Mahadevan-Jansen, Automated method for subtraction of fluorescence from biological Raman spectra, *Appl. Spectrosc.*, 2003, **57**(11), 1363–1367, DOI: 10.1366/000370203322554518.

27 A. P. Shreve, N. J. Cherepy and R. A. Mathies, Effective rejection of fluorescence interference in Raman spectroscopy using a shifted excitation difference technique, *Appl. Spectrosc.*, 1992, **46**(4), 707–711, DOI: 10.1366/0003702924125122.

28 D. Wei, S. Chen and Q. Liu, Review of fluorescence suppression techniques in Raman spectroscopy, *Appl. Spectrosc. Rev.*, 2015, **50**(5), 387–406, DOI: 10.1080/05704928.2014.999936.

29 J. Barker, C. Snape and D. Scurr, A novel technique for investigating the characteristics and history of deposits formed within high pressure fuel injection equipment, *SAE Int. J. Fuels Lubr.*, 2012, **5**(3), 1155–1164, DOI: 10.4271/2012-01-1685.

30 W. Meredith, *et al.*, Assessment of hydropyrolysis as a method for the quantification of black carbon using standard reference materials, *Geochim. Cosmochim. Acta*, 2012, **97**, 131–147, DOI: 10.1016/J.GCA.2012.08.037.

31 P. L. Ascough, *et al.*, Hydropyrolysis as a new tool for radiocarbon pre-treatment and the quantification of black carbon, *Quat. Geochronol.*, 2009, **4**(2), 140–147, DOI: 10.1016/J.QUAGEO.2008.11.001.

32 R. Caprotti, A. Breakspear, O. Graupner, T. Klaua and O. Kohnen, Diesel injector deposits potential in future fueling systems, *SAE [Tech. Pap.]*, 2006, DOI: 10.4271/2006-01-3359.

33 A. Dorner-Reisel, *et al.*, Wear behaviour of hydrogen free diamond-like carbon thin films in diesel fuel at different temperatures, *Diam. Relat. Mater.*, 2014, **44**, 78–87, DOI: 10.1016/J.DIAMOND.2014.01.013.

34 R. Dallanegra and R. Caprotti, Chemical composition of ashless polymeric internal diesel injector deposits, *SAE [Tech. Pap.]*, 2014, DOI: 10.4271/2014-01-2728.

35 J. Barker, J. Reid, C. Snape, D. Scurr and W. Meredith, Spectroscopic studies of internal injector deposits (IDID) resulting from the use of non-commercial low molecular weight polyisobutylenesuccinimide (PIBSI), *SAE Int. J. Fuels Lubr.*, 2014, **7**(3), 762–770, DOI: 10.4271/2014-01-2720.

36 J. Barker, *et al.*, Investigations of diesel injector deposits characterization and testing, *SAE [Tech. Pap.]*, 2020, DOI: 10.4271/2020-01-2094.

37 Z. Stępień, Types of internal Diesel injector deposits and counteracting their formation, *Combust. Engine.*, 2015, **163**(4), 79–91, DOI: 10.19206/CE-116859.

38 A. G. Rombolà, D. Fabbri, W. Meredith, C. E. Snape and A. Dieguez-Alonso, Molecular characterization of the thermally labile fraction of biochar by hydropyrolysis and pyrolysis-GC/MS, *J. Anal. Appl. Pyrolysis*, 2016, **121**, 230–239, DOI: 10.1016/j.jaap.2016.08.003.

39 W. Meredith, C. E. Snape and G. D. Love, Development and use of catalytic hydropyrolysis (HyPy) as an analytical tool for organic geochemical applications, *RSC Detect. Sci.*, 2014, **2015**(4), 171–208, DOI: 10.1039/9781782625025-00171.

40 C. E. Snape, *et al.*, Quantitative reliability of aromaticity and related measurements on coals by 13C n.m.r. A debate, *Fuel*, 1989, **68**(5), 547–548, DOI: 10.1016/0016-2361(89)90142-7.

41 F. Adar, A proposal for the origin of the near-ubiquitous fluorescence in Raman spectra, *Spectroscopy*, 2025, **40**(2), 8–12, DOI: 10.56530/SPECTROSCOPY.TA7090C5.

42 E. Cloutis, P. Szymanski, D. Applin and D. Goltz, Identification and discrimination of polycyclic aromatic hydrocarbons using Raman spectroscopy, *Icarus*, 2016, **274**, 211–230, DOI: 10.1016/J.ICARUS.2016.03.023.

43 H. Shen, L. Zhang, M. Liu and Z. Zhang, Biomedical applications of graphene, *Theranostics*, 2012, **2**(3), 283, DOI: 10.7150/THNO.3642.

44 M. A. Saeed, *et al.*, Graphene applications in composites, energy, and water treatment, *Macromol. Mater. Eng.*, 2025, **310**(4), 2400316, DOI: 10.1002/MAME.202400316.

45 F. Adar, Use of Raman spectroscopy to qualify carbon materials, *Spectroscopy*, 2022, **37**(6), 11–15, DOI: 10.56530/SPECTROSCOPY.WX3481U2.

46 F. Yang, S. Wang and Y. Zhang, Effects of laser power and substrate on the Raman shift of carbon-nanotube papers,

Carbon Trends, 2020, **1**, 100009, DOI: 10.1016/J.CARTRE.2020.100009.

47 H. Ferreira, *et al.*, Laser power influence on Raman spectra of multilayer graphene, multilayer graphene oxide and reduced multilayer graphene oxide, *J. Phys. Conf. Ser.*, 2018, **1143**(1), 012020, DOI: 10.1088/1742-6596/1143/1/012020.

48 C. Cong, T. Yu, R. Saito, G. F. Dresselhaus and M. S. Dresselhaus, Second-order overtone and combination Raman modes of graphene layers in the range of 1690–2150 cm^{-1}, *ACS Nano*, 2011, **5**(3), 1600–1605, DOI: 10.1021/NN200010M.

49 S. Piscanec, M. Lazzeri, F. Mauri, A. C. Ferrari and J. Robertson, Kohn anomalies and electron-phonon interactions in graphite, *Phys. Rev. Lett.*, 2004, **93**(18), 185503, DOI: 10.1103/PhysRevLett.93.185503.

50 F. Tuinstra and J. L. Koenig, Raman spectrum of graphite, *J. Chem. Phys.*, 1970, **53**(3), 1126–1130, DOI: 10.1063/1.1674108.

51 J. Ullmann, M. Geduldig, H. Stutzenberger, R. Caprotti and G. Balfour, Investigation into the formation and prevention of internal diesel injector deposits, *SAE [Tech. Pap.]*, 2008, DOI: 10.4271/2008-01-0926.

52 J. Barker, C. Snape and D. Scurr, Information on the aromatic structure of internal diesel injector deposits from time of flight secondary ion mass spectrometry (ToF-SIMS), *SAE [Tech. Pap.]*, 2014, DOI: 10.4271/2014-01-1387.

53 J. Barker, P. Richards, D. Pinch and B. Cheeseman, Temperature programmed oxidation as a technique for understanding diesel fuel system deposits, *SAE Int. J. Fuels Lubr.*, 2010, **3**(2), 85–99, DOI: 10.4271/2010-01-1475.

54 L. M. Wenger, C. L. Davis, J. M. Evensen, J. R. Gormly and P. J. Mankiewicz, Impact of modern deepwater drilling and testing fluids on geochemical evaluations, *Org. Geochem.*, 2004, **35**(11–12), 1527–1536, DOI: 10.1016/J.ORGGEOCHEM.2004.07.001.

55 M. A. Sephton, W. Meredith, C. G. Sun and C. E. Snape, Hydropyrolysis as a preparative method for the compound-specific carbon isotope analysis of fatty acids, *Rapid Commun. Mass Spectrom.*, 2005, **19**(3), 323–325, DOI: 10.1002/RCM.1788.

56 A. C. Ferrari and J. Robertson, Raman spectroscopy of amorphous, nanostructured, diamond-like carbon, and nanodiamond, *Philos. Trans. A Math. Phys. Eng. Sci.*, 2004, **362**(1824), 2477–2512, DOI: 10.1098/rsta.2004.1452.